Nonlinear Carrier Interactions in Lead Halide Perovskites and the Role of Defects

Ajay Ram Srimath Kandada,[†,∥] Stefanie Neutzner,[†,‡,∥] Valerio D'Innocenzo,[†,‡] Francesco Tassone,[†] Marina Gandini,[†,‡] Quinten A. Akkerman,[§,⊥] Mirko Prato,[§] Liberato Manna,[§] Annamaria Petrozza,*,[†] and Guglielmo Lanzani[†,‡]

[†]Center for Nano Science and Technology @Polimi, Istituto Italiano di Tecnologia, via Giovanni Pascoli 70/3, 20133 Milano, Italy
[‡]Dipartimento di Fisica, Politecnico di Milano, Piazza Leonardo da Vinci, 32, 20133 Milano, Italy
[§]Nanochemistry Department, Istituto Italiano di Tecnologia, Via Morego 30, 16163 Genova, Italy
[⊥]Dipartimento di Chimica e Chimica Industriale, Università degli Studi di Genova, Via Dodecaneso 31, 16146 Genova, Italy

Ⓢ *Supporting Information*

ABSTRACT: The simple solution processability at room temperature exposes lead halide perovskite semiconductors to a non-negligible level of unintentional structural and chemical defects. Ascertained that their primary optoelectronic properties meet the requirement for high efficiency optoelectronic technologies, a lack of knowledge about the nature of defects and their role in the device operation currently is a major challenge for their market-scale application due to the issues with stability and reliability. Here, we use excitation correlation photoluminescence (ECPL) spectroscopy to investigate the recombination dynamics of the photogenerated carriers in lead bromide perovskites and quantitatively describe the carrier trapping dynamics within a generalization of the Shockley−Read− Hall formalism. The superior sensitivity of our spectroscopic tool to the many-body interactions enables us to identify the energetics of the defects. In fact, in the case of polycrystalline films, depending on the synthetic route, we demonstrate the presence of both deep and shallow carrier traps. The shallow defects, which are situated at about 20 meV below the conduction band, dope the semiconductor, leading to a substantial enhancement of the photoluminescence quantum yield despite carrier trapping. At excitation densities relevant for lasing, we observe breakdown of the rate-equation model, indicating a buildup of a highly correlated regime of the photocarrier population that suppresses the nonradiative Auger recombination. Furthermore, we demonstrate that colloidal nanocrystals represent virtually defect-free systems, suffering from nonradiative quenching only due to subpicosecond Auger-like interactions at high excitation density. By correlating the fabrication conditions to the nonradiative loss channels, this work provides guidelines for material engineering towards superior optoelectronic devices.
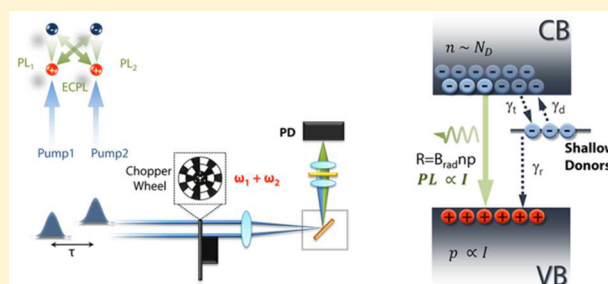
INTRODUCTION

Lead halide perovskite semiconductors have shown their potential application in a variety of optoelectronic technologies due to their high refractive index, excellent light-harvesting capability, and suitable emission and optical gain properties.[1] They have a direct band gap in the visible energy range, with large oscillator strength associated with an excitonic transition close to the band edge.[2] Efficient screening results in binding energies ranging from a few to tens of millielectronvolts,[3,4] and, accordingly, at room temperature and excitation densities relevant for photovoltaic and light emitting devices, that is, below $10^{17} cm^{-3}$, there is predominant population of ionized states (electron−hole plasma).[3,5] However, the free carriers are highly susceptible to trapping at defects associated with intragap states, limiting the device performances. This gives rise to a density-dependent branching of the recombination paths and strongly influences the carrier lifetimes and photoluminescence quantum yields (PLQY). Although PLQY

up to 90% has been demonstrated in well-passivated colloidal nanocrystals,[6,7] polycrystalline thin films have PLQYs hardly above 30% at excitation densities below $10^{17} cm^{-3}$.[8] Furthermore, at high excitation densities ($>10^{17} cm^{-3}$), typical for the lasing regime, many-body Auger recombination opens a new channel for the population loss.[9,10] For an effective device optimization, it is important to comprehend and quantify the limiting mechanisms influencing the carrier dynamics.

On the basis of time-resolved PL (Tr-PL) spectroscopy measurements at different experimental conditions, the recombination dynamics in methylammonium lead iodide ($MAPbI_3$) and bromide ($MAPbBr_3$) perovskites have been largely described within the Shockley−Read−Hall (SRH) framework,[9,11,12] wherein the carriers are assumed to be trapped at deep defect states within the band gap. Accordingly,

the population dynamics are described by a simple rate equation, $\frac{dn}{dt} = G - k_1 n - k_2 n^2$, where G is the generation rate, and k_1 and k_2 are the monomolecular trapping and bimolecular radiative recombination rates, respectively. However, given the varied nature of defects that the perovskite films are prone to, such a simplistic description may not suffice to provide a comprehensive photophysical picture. There is experimental[13,14] and theoretical evidence[15−20] for the existence of both shallow and deep level traps arising from an assortment of point, surface, or linear defects, with each of them displaying distinct photophysical characteristics. For example, charged shallow defects may dope the material and not necessarily form recombination centers, while neutral deep traps act as nonradiative quenchers of the excited-state population. Importantly, it has been suggested that their selective manifestation in the film is governed by the specific precursor chemistry at the fabrication stage,[15,21,22] as well as the postfabrication conditions.[23−25]

Hysteretic behaviors and low conductivity of polycrystalline perovskite thin films make electrical measurements for defect characterization hard to perform and difficult to interpret. Conventional PL techniques also fail to capture such rich but complex defect physics, due to their inability to identify the nature of carrier traps unambiguously and model free. Although they enable the measurement of various recombination rates, including the trapping rates, they do not distinguish between different kinds of traps and possible doping and excitonic effects, which are left as variable outcomes of numerical analysis of the decays.[13] Measurements of intensity-dependent steady-state quantum yields can give crucial hints in choosing appropriate photophysical scenarios;[5,21] yet they are seldom performed in conjunction with the time-resolved measurements. The variability of the nature and density of defects with the fabrication route and experimental conditions adds complexity to the problem and calls for methods that can intrinsically distinguish myriad nonradiative decay paths.

In this work, we employ ECPL spectroscopy,[26−28] an all optical method, which has inherent sensitivity to the nonlinear interactions among the excited carriers and thus provides unique insights into the nonradiative decay channels. We investigate the recombination dynamics in lead bromide perovskites and explore the influence of the fabrication route. In polycrystalline thin films of MAPbBr$_3$, where the perovskite is crystallized directly on the substrate as in most of the operating devices, we demonstrate the presence of both deep trap states as well as shallow defects, which induce unintentional doping and quantitatively assess their influence on the density-dependent recombination dynamics. Their respective manifestation depends on the fabrication protocol; in particular, we note that an excess of halogen mitigates the presence of detrimental deep trap states. In fact, in the alternative case of CsPbBr$_3$ nanocrystals, which are grown as colloids in the presence of excess halogen, we observe that the recombination mechanism is dominated by radiative electron−hole recombination, thus demonstrating that there is no intrinsic limitation in the material performances. However, they still suffer from nonradiative Auger recombination when the average number of photoexcitations per nanocrystal exceeds ∼0.15, depleting the population in the subpicosecond time scale.

RESULTS AND DISCUSSION

We first perform ECPL experiments on MAPbBr$_3$ perovskite thin films prepared by two different fabrication routes. MA-1 is fabricated with equimolar material precursors (PbBr:MABr− 1:1) in a single step, while MA-2 is obtained in the presence of an excess of MABr (1:1.05). The UV−vis absorption and cw-PL spectra of these samples, reported in Figure 1a and b, show
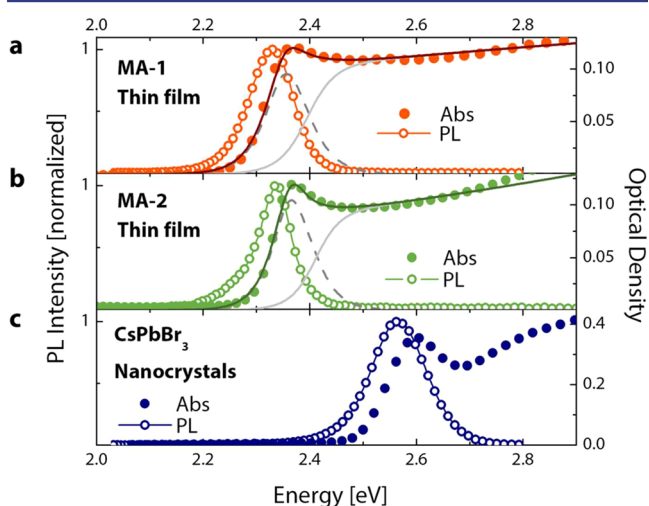

Figure 1. UV−vis absorption and PL spectra of (a) MA-1 and (b) MA-2 thin films made with different precursor concentrations and of (c) colloidal suspension of CsPbBr$_3$ nanocrystals. Plotted as gray lines in the top two panels are the free carrier and excitonic absorption spectra obtained from Elliott analysis of the total absorption.

that they exhibit very similar optical characteristics. Both of the films are characterized by an absorption onset at approximately 2.35 eV, with an excitonic resonance at 2.37 eV. Following Elliott analysis (see section S1) of the absorption spectra, we obtain very similar exciton binding energies of 42 and 47 meV for MA-1 and MA-2, respectively. We compare these samples with a colloidal suspension of CsPbBr$_3$ cubic nanocrystals of approximate size of 7 nm. The nanocrystals have a blue-shifted band-edge and a stronger excitonic peak, due to the non-negligible quantum confinement (Figure 1c). The PL values from all of the samples are Stokes shifted by about 30 meV with respect to the excitonic transition in the linear absorption. We note that MA-1 exhibits a very low PLQY of <1% at excitation densities slightly greater than 10^{16} cm^{-3}, while MA-2 shows a higher yield of about 4% at similar densities (and under ambient atmosphere). This is in line with recent reports, which show that the presence of excess Br at the fabrication stage results in films with higher luminescence yields, although this observation has not been categorically rationalized.[29] On the other hand, NCs show a very high PLQY of about 75%, representing a very efficient system for light emission. The structural analysis of the samples is shown in section S1.

In the ECPL experiment (schematically represented in Figure 2), we measure the time integrated PL upon photoexcitation with two temporally delayed pump pulses of equal intensity, I_{pump}, and energy, 3.1 eV. The total intensity of the collected PL in the presence of both of the pulses can be written as:[27]
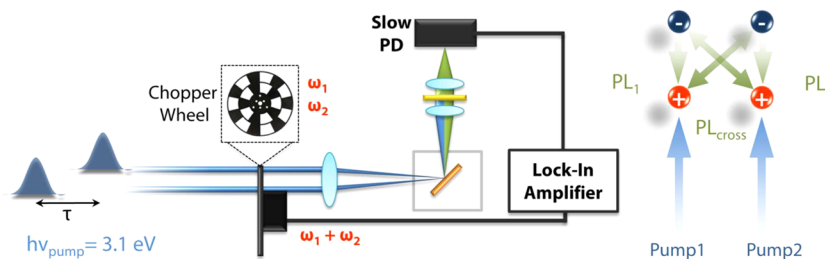
Figure 2. Schematic representation of the excitation correlation photoluminescence (ECPL) experiment.
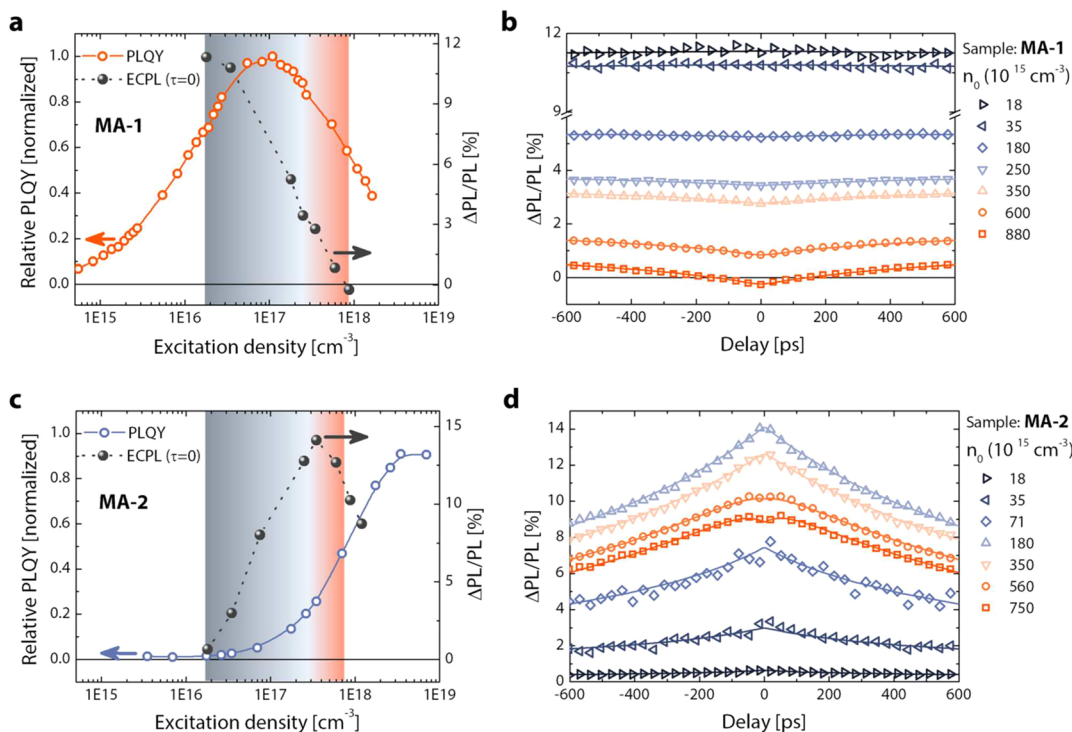

Figure 3. (a) MA-1 and (c) MA-2: relative PLQY and zero-delay ECPL signal plotted as a function of excitation density. (b) MA-1 and (d) MA-2: ECPL dynamics at different excitation densities; experimental data are plotted as symbols, while the solid lines are the numerical fits.

$$\mathrm{PL}(2I_{\mathrm{pump}}, \tau) = \int_0^\infty \mathrm{PL}_1(I_{\mathrm{pump}}, t)\, \mathrm{d}t$$

$$+ \int_\tau^\infty \mathrm{PL}_2(I_{\mathrm{pump}}, t)\, \mathrm{d}t$$

$$+ \int_\tau^\infty \mathrm{PL}_{\mathrm{cross}}(2I_{\mathrm{pump}}, t, t - \tau)\, \mathrm{d}t \tag{1}$$

where τ is the delay between the pulses. The first two terms in eq 1 represent the PL due to each of the pump pulses separately, while the third term arises from the nonlinear mixing of the photoexcited population. The ECPL signal represents the fraction of this nonlinear term over the total PL and thus can be written simply as $\mathrm{ECPL}(\tau = 0, I_{\mathrm{pump}}) = \frac{\mathrm{PL}(2I_{\mathrm{pump}}) - 2\mathrm{PL}_1(I_{\mathrm{pump}})}{\mathrm{PL}(2I_{\mathrm{pump}})}$, at zero-delay between the pulses. By scanning the delay between the pulses, we obtain the photoexcitation dynamics with a temporal resolution limited only by the pulse-width, in the present case, ~150 fs. Being a lock-in-based heterodyne technique (see Experimental Methods), ECPL also offers higher S/N ratios in comparison to the conventional streak camera or photon counting systems.

An ideal scenario of pure radiative regime, with either geminate ($\frac{dn}{dt} = -An + G$) or bimolecular ($\frac{dn}{dt} = -Bn^2 + G$) recombination, results in a linear growth of steady-state PL with the excitation density. According to eq 1, this will give rise to a null ECPL signal. The presence of density-dependent competing nonradiative channels bestows a superlinear or sublinear behavior of the PL with intensity, resulting in a nonzero ECPL signal. For example, within the SRH formalism with deep traps, the PL increases with intensity as $I^{1.5}$ (see section S2 for a detailed analysis). In such a scenario, the largest, positive, ECPL signal achievable is approximately 30%, at $\tau = 0$ delay. Auger-like processes yield a sublinear dependence of the PL on the intensity ($I^{0.6}$) and give rise to a negative ECPL peak. Thus, ECPL specifically picks out the contribution of the limiting nonradiative channels from the overall recombination dynamics and provides greater precision in the analysis than conventional techniques.

Figure 3a and c shows the relative PLQY (see Experimental Methods) plotted as a function of the excitation density for MA-1 and MA-2, respectively. The trends of ECPL taken at zero-delay between the pulses are also shown for both of the samples. In Figure 3b and d, we show the ECPL dynamics

taken at different excitation densities, for MA-1 and MA-2, respectively. The symmetry in the dynamics along the zero-delay is due to the reciprocity of the two pulses.

We first consider the case of the MA-1 thin films whose relative PLQY exhibits a monotonic increase with the excitation density (Figure 3a). This clearly indicates the density-dependent quenching of the nonradiative path, here assigned to the trapping of the photogenerated carriers. As the excitation density becomes closer to and then above the available trap density, most of the traps are filled, leaving substantial free-carrier population for radiative recombination resulting in higher PLQY. At very large densities (close to 10^{18} cm^{-3}), additional nonradiative channels open, reducing the yield.

At an excitation density of about 10^{16} cm^{-3}, we observe an ECPL signal of about 11% (Figure 3a and b), which exhibits no decay at least within the 600 ps window. The positive sign of the signal fits well with the trap limited behavior as discussed earlier. The lack of any dynamics in the measured time range indicates that recombination lifetimes are on the nanosecond time scale. As the excitation density is further increased, the system moves toward the linear radiative regime due to trap filling, reducing the ECPL signal. At excitation densities beyond 3×10^{17} cm^{-3}, a kinetic appears in the ECPL time trace with the signal becoming negative close to the zero-delay and at the highest excitation density used. We assign this to the nonradiative Auger recombination process, and accordingly the observed dynamics directly corresponds to the Auger rate.

Moving to the case of MA-2 film, we find that the intensity dependence of the relative PLQY, shown in Figure 3c, follows a trend similar to that of MA-1, highlighting again a trap-limited recombination process, albeit it remains pretty insensitive to excitation intensity, over about two decades, before increasing. Note that the absolute PLQY is considerably higher in this case than in MA-1. The ECPL is however suggesting a different, and an apparently contradicting, scenario. First, the ECPL response, shown in Figure 3c and d, is close to zero at low excitation densities, which, in complete contrast to the case of MA-1, suggests a trapless efficient radiative recombination. Second, the ECPL increases to a maximum of about 15% upon increasing the excitation density up to 10^{17} cm^{-3}. Note in addition that at all of the excitation densities, there is a distinct ECPL dynamic with decay time of about 500 ps. At excitation densities above 3×10^{17} cm^{-3}, the ECPL signal drops and a negative dip develops around zero-delay.

For a quantitative analysis of the intensity and the dynamics of the ECPL, we consider a comprehensive model detailed within the set of rate eqs 2−4 and schematically represented in Figure 4.

$$\frac{dn}{dt} = G - R - \gamma_t(N_t - n_t)n + \gamma_d n_t - \gamma_{Auger}n^2 p \quad (2)$$

$$\frac{dp}{dt} = G - R - \gamma_r n_t p - \gamma_{Auger}n^2 p \quad (3)$$

$$\frac{dn_t}{dt} = \gamma_t(N_t - n_t)n - \gamma_r n_t p - \gamma_d n_t \quad (4)$$

In eqs 2−4, G is the generation rate, given by the light absorption. $R = B_{rad}np$ represents the radiative bimolecular recombination dictated by the recombination coefficient B_{rad}. γ_t represents the carrier-trapping rate, and we assume predominant electron trapping; N_t represents the total available trap density; γ_r represents the nonradiative recombination of the
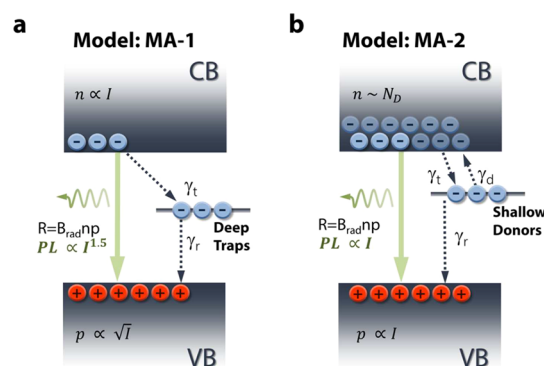

Figure 4. (a) Photophysical scenario of MA-1 with deep trap as the primary nonradiative channel. (b) Model used for MA-2, with shallow donors that dope the material and also act as nonradiative recombination centers.

trapped electron with hole; γ_d is the detrapping rate: if the electron (hole) is trapped within a deep level, this rate is negligible, while in the case of shallow traps, this term cannot be neglected. γ_{Auger} represents the nonradiative Auger rate that is relevant at higher densities. For the sake of simplicity, we assume that the electrons are predominantly trapped, although the model can be easily extended even for hole traps. Unlike the usual formalism used in the literature, which considers only the dynamical evolution of the carrier population with a monomolecular trapping rate, we consider a set of coupled equations accounting for electron, hole, and trap densities, with no presumptions on the nature of carrier trapping.

By fitting the ECPL of MA-1 with such a model, we obtain a trap density of around 1×10^{17} cm^{-3}; $B_{rad} = 2 \times 10^{-9}$ cm^3 s^{-1}; $\gamma_{Auger} = 1 \times 10^{-27}$ cm^6 s^{-1}; $\gamma_t = 0.84 \times 10^{-9}$ cm^3 s^{-1}; and $\gamma_r = 0.19 \times 10^{-9}$ cm^3 s^{-1} (the complete list of parameters is listed in section S3.1). Overall, these experiments provide a quantitative description of the trap limited electron−hole recombination for perovskites within the SRH framework, as was already proposed in previous studies.[12,13]

If we employ the same photophysical model (Figure 3c, with deep traps) to fit the ECPL response of MA-2 at low density ($\sim 18 \times 10^{15}$ cm^{-3}), we retrieve an extremely high B_{rad} of about 2.2×10^{-6} cm^3 s^{-1}. This is about 3 orders of magnitude higher than that of MA-1, and it would give rise to a PLQY of almost unity. More importantly, to account for the increase of the ECPL signal (Figure 3c) and to fit the dynamics at higher excitation densities, we would need to introduce an inverse density dependence for this coefficient (see section S3.2). B_{rad} is however an intrinsic material property, correlated to the electronic structure through its dependence on the bandgap and the transition moments between the bands.[30] Thus, with similar chemical composition and identical optical signatures, MA-2 must exhibit a B_{rad} similar to that of MA-1 and show no dependence on the excitation density. This makes the fit unphysical, and calls for a refinement of the photophysical scenario.

Virtually null ECPL response suggests an almost linear dependence of PL ($\propto B \cdot n \cdot p$) on intensity at low density, instead of the 3/2 power of the previous case. Such a linear dependence in the presence of trapping process can be explained by assuming the existence of shallow donors (or acceptors), which are thermally ionized to dope the material, apart from creating nonradiative recombination centers (represented in Figure 4b). Doping manifests itself in the

charge neutrality condition as $n + n_t = N_D + p$ (where n, p, n_t, and N_D are the electron, hole, filled trap, and doping densities, respectively), resulting in a large background doping $n \cong N_D$, even in the dark. Supposing the shallow defects are n-doping the material, at low excitation density p is proportional to the light intensity I and $n \cong N_D$. PL is linear with excitation intensity I because it stems from the radiative recombination of the photogenerated holes ($p \approx I$) and the doping electrons ($n \cong N_D$). Accordingly, the ECPL response (see section S2.4) is negligibly small. At higher intensity, the photogenerated electron density becomes comparable to background doping and thus participates in the radiative process albeit in competition with carrier trapping, which results in a positive ECPL signal. It can be shown analytically that the zero-delay ECPL response increases almost linearly with excitation density (section S2.4). This can be directly perceived in the linear trend of the zero-delay ECPL signal until an excitation density of about 10^{17} cm^{-3} in Figure 4a, with the onset and slope of the rise dictated by the doping concentration. Note that such a background doping and presence of shallow traps mitigate the nonradiative losses, which can in fact explain the higher PLQY observed in MA-2 with respect to MA-1.

We performed a quantitative analysis of the ECPL dynamics of MA-2 with the set of eqs 2−4], considering the modified charge neutrality condition accounting for doping, and a non-negligible detrapping rate, relevant for a shallow traps as illustrated in Figure 4b. We note that the observed ECPL dynamics here correspond mainly to the subnanosecond trapping by the available shallow donor states. The complete list of the resulting parameters is reported in section S3.3. We retrieve a donor density of about 2×10^{18} cm^{-3} and a trapping rate, γ_t, of 3×10^{-8} cm^3 s^{-1}, which are much higher than in the case of MA-1, in agreement with the shift of the relative PLQY slope to higher excitation density. Importantly, the estimated value of B_{rad} is now back to the value found in MA-1 as expected for an intrinsic characteristic of the material.

Ionization of the donor/acceptor states, responsible for the doping, is a thermal mediated process. The doping density (N_D) is hence proportional to the term: $\exp(\Delta E_d/kT)$, where ΔE_d is the energy of the defect state within the bandgap with respect to the bottom of the electronic bands and represents the defect ionization energy. Following such a relation, one would expect a reduced doping concentration at lower temperatures. Because the ECPL signal follows the ratio between the excitation density and the background doping (see section S2.4), this would increase the ECPL response. To verify this, we performed measurements at 77 K, and in Figure 5a we show the intensity dependence of the zero-delay ECPL signal at 77 K plotted along with the signal taken at 290 K. At a fixed low excitation density of about 3×10^{15} cm^{-3}, we find that (i) the ECPL response increases from 0.8% at 290 K to about 8% at 77 K and (ii) the progressive ECPL trend shifts to lower excitation densities at 77 K with respect to the RT case. Both observations are in good agreement with the expected reduction in background doping. From the amount of shift, we can roughly write the doping concentration at 77 K as $N_D(77$ K$) \approx 0.1 N_D(290$ K$)$, from which we can make a quick estimation of the defect ionization energy as about 20 meV. The inverse proportionality between the ECPL signal and the doping concentration leads to a linear relationship beween ln(ECPL) and $1/kT$ as shown in Figure 5b, with the measurement performed at a fixed excitation density of 3×10^{15} cm^{-3}. The slope of this curve is given by ΔE_d, which can be fitted to be 19
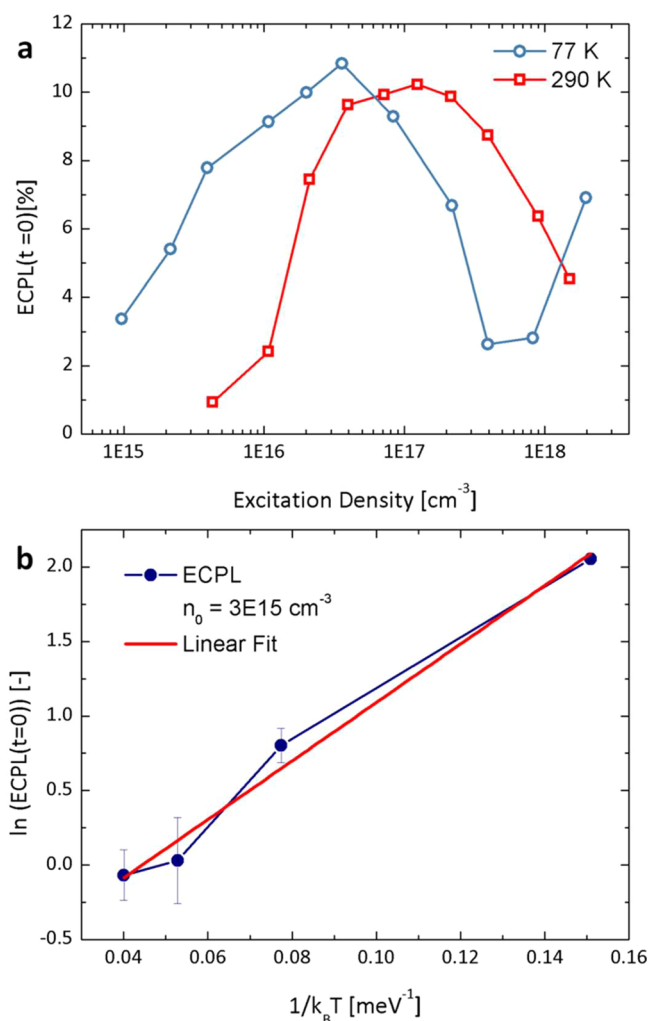

Figure 5. (a) MA-2: Intensity dependence of time-zero ECPL signal at 77 and 290 K. (b) Natural logarithm of the time-zero ECPL signal taken at a fixed excitation density of 3×10^{15} cm^{-3}, plotted against $1/k_BT$ where k_B is the Boltzmann constant and T is the temperature.

± 1.7 meV, in agreement with our assumption of shallow defects. Interestingly, a recent report by Cho et al.[29] shows that when MAPbBr$_3$ thin films are synthesized in the presence of excess of MABr, the work function of the semiconductor is reduced.

Recent theoretical works have primarily suggested that most of the intrinsic point defects in lead halide perovskites form shallow carrier traps.[17,31−33] Because of the large formation energies theoretically predicted for the deep defect states, their role in the carrier recombination must be negligible. This is in agreement with our observation in MA-2, where the primary carrier traps are shallow defects. Nevertheless, formation of deep defects that are associated with the halogen has also been suggested.[16,34] Buin et al.[15] have in fact shown under "halogen-poor" conditions in MAPbBr$_3$ that Br vacancies form deep trap states with large ionization energies. This is in agreement with the recombination dynamics of MA-1 sample presented here, which is more prone to Br vacancies than MA-2, that is on the contrary prepared in a "halogen-rich" condition. Therefore, although independent experiments to identify the chemical origin/nature of defect states are still needed, ECPL is able to provide their energetics (i.e., shallow vs deep), thus providing indications of their impact on the optoelectronic processes in
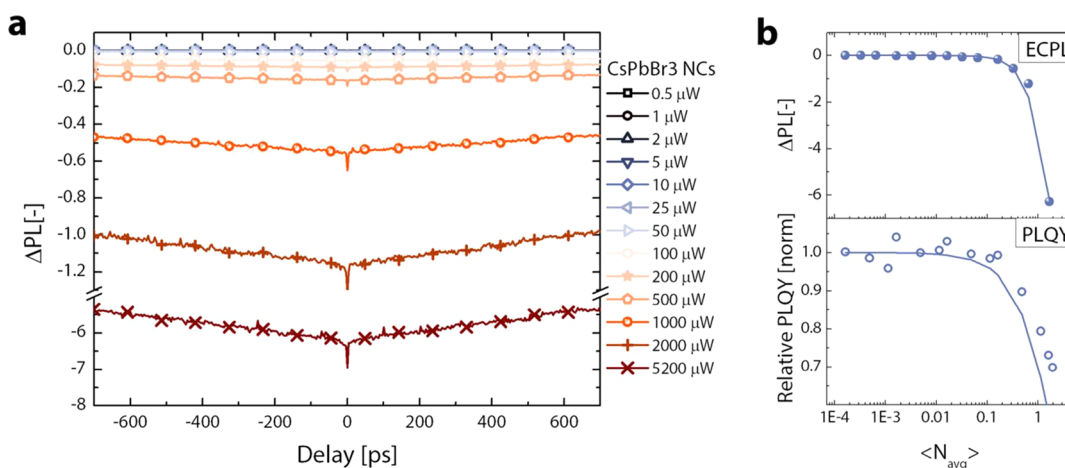
Figure 6. (a) ECPL dynamics of a colloidal suspension of $CsPbBr_3$ nanocrystals taken at different pump intensities. (b) ECPL (top panel) and relative PLQY (bottom panel) plotted as a function of the average number of excitations per particle. The experimental data are plotted as symbols, and theoretical estimates (see main text) are plotted as solid lines.

the thin films and a direction for further combined chemical and theoretical investigations.

Moving to the analysis of the ECPL signal beyond excitation densities of 10^{17} cm^{-3} in the case of MA-2, we note that the model breaks down and it is unable to account for the drop in ECPL signal. Indeed, keeping B_{rad} fixed leads to a growing ECPL signal well above the observed maximum value of 15%. By considering Auger nonradiative recombination to reverse this trend, an abrupt drop in the PLQY is predicted, but it is not observed.

The new regime in MA-2 at high excitation density could be explained by a density-dependent renormalization of the carrier−carrier interaction screening leading to the increase in carrier correlation. This would result in the formation of an exciton population or strongly correlated electron−hole plasma, which reduces the interactive term in eq 1. Coalescence of carriers into a stable exciton requires the release of the energy to the lattice. In this material, the expected binding energy is 3−5 times larger than the LO phonon energy at thermodynamic equilibrium, requiring a multi phonon emission process that is quite unlikely. However, the exciton binding energy reduces with carrier density, as a result of e−h plasma screening. A simple estimate of the bandgap renormalization[35] from screening gives ~60 meV at 3×10^{17} cm^{-3}, and ~100 meV at 10^{18} cm^{-3} with the typical square root scaling with density. Therefore, just in the density range of the peculiar ECPL response, exciton formation could occur via the emission of a single LO phonon. This process could thus occur with higher probability than any other multiphonon phenomena. Note that this interpretation is fairly robust because at slightly larger densities, Mott transition occurs, with the full disappearance of the exciton binding, but still preserving the geminate recombination path. Our explanation is qualitative, because the carrier density is quickly decreasing in time, leading to the superposition of different regimes and the simultaneous interplay between screening, Mott transition, and eventually exciton formation. While these complex dynamics are clearly well beyond the simple free-carrier model presented in eqs 2−4), our results capture the essence of the carrier interactions in perovskites under different regimes. The selective expression of the geminate regime only in MA-2 can be partly related to higher film quality with lower deep trap density. This may in

turn reduce the Auger scattering, thus enabling a substantial carrier population to be available for radiative recombination.

We also note that all of the measurements reported in Figure 3 are carried out on samples that are kept under constant illumination of high intensity pulses before starting the experiment and in a vacuum, to reduce PL instabilities. Indeed, before stabilizing, the PLQY reduces in minutes, and accordingly the ECPL at a fixed excitation intensity increases (Figures S2 and S3). This indicates that the available trap density is increasing on very slow time scales, possibly associated with photoinduced formation of deep-trap complexes as suggested by Agiorgousis et al.[16]

Having investigated the role of defects in thin films, we turn our attention toward colloidal suspensions of nanocrystals (NCs) of $CsPbBr_3$. They exhibit PLQY as high as 75%, even at low excitation densities,[6,36] and monoexponential PL decay kinetics with a lifetime of about 4 ns, suggesting pure excitonic emission.[36] This already indicates a minimum role of defects in the photocarriers dynamics; thus this set of samples can first be used as a control case to validate our experimental methodology in assessing the carrier trapping process. Note that, changing the cation from MA^+ to Cs^+, the thin films exhibit characteristics similar to those of the MA-2 sample (see Figure S4), and thus we are not introducing additional variability. We consider here nanocrystals with an average size of 6.7 ± 1 nm, whose UV−vis absorption and PL spectra are reported in Figure 1.

In Figure 6a, we report the ECPL collected from the NCs sample at different excitation intensities. Under low excitation, we obtain a zero ECPL response substantiating the efficient excitonic nature of the emission. As the pump intensity is increased, the signal becomes negative monotonically, however keeping the same kinetics. The negative ECPL response can be attributed to Auger-like quenching of the excited-state population in the ultrafast time scales. This is in fact even more evident when looking at the dynamics close to the time-zero, which shows an ultrafast decay (<250 fs).

In the case of the NCs, it is intuitive to estimate the average number of excitations per nanocrystal rather than excitation density. Assuming that that the value of absorptivity (α in cm^{-1}) at 3.1 eV (corresponding to bulk carrier absorption) for NCs is similar to that of the film, which is evaluated to be around 10^4 cm^{-1}, the average number of carriers on each

nanocrystal can be evaluated as $\langle N \rangle = \sigma \phi_{photon}$, where $\sigma = \alpha V$ (V is the volume of the NC) is the cross-section and φ_{photon} is the photon flux. We obtain a cross section of about 3×10^{-15} cm², in agreement with the estimates of Makarov et al.[37] As shown in Figure 6b, the negative ECPL starts to increase significantly when $\langle N \rangle > 0.15$. This approximately coincides with the carrier density at which the PLQY starts to drop from its maximum value.

When the number of the photoexcitations per particle exceeds one, Auger interactions bring the population back to less than one within 1 ps. Therefore, after certain pump intensity, only one photon is emitted irrespective of the injected density. Overall the fast nonradiative de-excitation results in a saturation of the PL emission, as was also seen as a reduction of the relative PLQY in Figure 6b. As a consequence, the first pump pulse will saturate the PL emission, and the photoexcitations created by the delayed pulse are quenched by the ultrafast Auger interactions resulting in detrimental contribution to the PL ($\Delta PL < 0$). The PL decays with the intrinsic exciton lifetime, thus resulting in a monoexponential ECPL dynamics independent of the pump intensity.

The trends shown in Figure 6b can be analytically reproduced by considering the probability (p_m) of finding m excitons in a nanocrystal, given by a Poisson distribution $p_m = \frac{\langle N \rangle^m}{m!} e^{-\langle N \rangle}$. Following ultrafast Auger recombination, each photoexcited nanocrystal is left with only one exciton for radiative recombination. In such a scenario, PL is proportional to the sum, $(p_1 + p_2 + ...) = 1 - p_0 = 1 - e^{-\langle N \rangle}$.[38] Accordingly, we can estimate PLQY as $\frac{1 - e^{-\langle N \rangle}}{\langle N \rangle}$ and ECPL as $(1 - e^{-2\langle N \rangle}) - 2(1 - e^{-\langle N \rangle})$, which are plotted as solid lines in Figure 6b,[39] and they closely follow the experimental trends. It must be noted that Auger recombination occurs before the onset of optical gain and hence presents the main limiting channel in lasing applications, as was also shown recently by Makarov et al.[37] On the contrary, in the low excitation density regime, the NCs represent a clean material system with no detrimental trapping processes reducing the yield.

CONCLUSIONS

In this work, we quantitatively assess the impact of defects and unintentional doping on the carrier dynamics in lead bromide perovskites by exploiting ECPL to extract the nonlinear part of the recombination process. The polycrystalline films of MAPbBr₃ synthesized by using a virtually equimolar concentration of the precursors exhibit SRH-like recombination mediated by the presence of deep carrier traps. On the contrary, the sample synthesized in the presence of an excess of MABr shows clear evidence of shallow defects. In particular, we show that these shallow defects are located approximately 20 meV below the conduction band, and they can be ionized leading to the doping of the crystal and in turn partly alleviate the nonradiative quenching of the carrier population. Our results thus demonstrate a correlation between the energetics of defect states (i.e., shallow versus deep), which affects the photocarrier dynamics in the semiconductor and the fabrication route of thin film. Although further and detailed studies are still needed to identify the "chemical" origin of such defects, our study provides the mechanistic framework to engineer materials with high optoelectronic quality. We also quantitatively fit the ECPL dynamics with appropriate photophysical models and obtain a set of relevant photophysical constants, such as

bimolecular recombination coefficient, $B_{rad} \approx 2 \times 10^{-9}$ cm³ s⁻¹, and Auger rate, $\gamma_{Auger} \approx 1 \times 10^{-27}$ cm⁶ s⁻¹, which compete above densities of 10^{18} cm⁻³. Furthermore, we report here for the first time a highly correlated regime of the carrier population, where geminate recombination becomes predominant, as long as the role of nonradiative recombination centers is mitigated. This is assigned to a renormalization of the band gap due to screening at high excitation density that competes and somehow limits the Auger recombination loss, otherwise detrimental for lasing applications. Finally, we demonstrate that colloidal nanocrystals provide a handle to create defect-free perovskites, although they still suffer from ultrafast Auger recombination that quenches the PL in the high excitation regime.

■ EXPERIMENTAL METHODS

Sample Preparation. *MAPbBr₃ Thin Films: MA-1.* The equimolar solution of lead bromide (PbBr₂) and methylammonium bromide (CH₃NH₃Br) is prepared in anhydrous N,N-dimethylformamide (20 wt %) and spin coated on clean glass at 3000 rpm for 60 s, and immediately annealed at 100 °C for 15 min.

MA-2. A solution of PbBr₂ and CH₃NH₃Br with a molar ratio of inorganic to organic of 1:1.05 is prepared in anhydrous dimethyl sulfoxide (40 wt %). The sample is prepared following the nanocrystal pinning recipe reported by Cho et al.[29] The spin-coating speeds used were 500 rpm for 7 s and 3000 rpm for 90 s. After the initial acceleration, the perovskite solution is dropped on the substrate. After 60 s, nanocrystal pinning is initiated by chlorobenzene. The sample is subsequently annealed at 90 °C for 10 min. All of the samples are encapsulated in a poly methyl methacrylate film before being exposed to ambient conditions.

CsPbBr₃ Nanocrystals. The colloidal suspensions are prepared as described by Akkerman et al.[6]

Excitation Correlation PL. The laser system consists of a mode:locked Ti:sapphire oscillator (Coherent Micra) that provides ~20 fs pulses centered around 800 nm at 80 MHz. The pulses are amplified using a regenerative amplifier (Coherent RegA 9000) at 250 kHz and compressed using a grating-based compressor to generate ~50 fs pulses with a pulse energy of 6 μJ. Pump pulses for the ECPL experiment are generated via frequency doubling of the 800 nm pulses in a BBO crystal. The beam is then split using a thin beam splitter to generate two pump pulses with one of them sent through a computer-controlled translation stage to achieve variable delay between them. Each of the pump pulses is modulated at distinct frequencies (381 and 272 Hz) using an optical chopper. They are then focused onto the sample with a lens of focal length ~150 mm. The PL from the sample is then collected onto a slow silicon photodiode, after filtering out the pump with a long-pass optical filter. The output of the photodiode is simultaneously fed into a lock-in amplifier and an oscilloscope to measure ΔPL and PL, respectively. The lock-in amplifier is referenced at the sum frequency (653 Hz) to selectively measure the fractional PL due to nonlinear interactions.

Relative PLQY. The excitation source is the same as in the ECPL experiment. The PL is collected and focused into a fiber coupled to a spectrometer (Ocean Optics Maya pro 2000). To obtain relative PLQY at each excitation density, the spectrally integrated PL is divided by the pump power.

■ ASSOCIATED CONTENT

ⓈSupporting Information

The Supporting Information is available free of charge on the ACS Publications website at DOI: 10.1021/jacs.6b06463.

    Section S1, sample characterization; section S2, how to interpret ECPL response; and section S3, ECPL fitting results (PDF)

■ AUTHOR INFORMATION

Corresponding Author

*annamaria.petrozza@iit.it

Author Contributions

‖A.R.S.K. and S.N. contributed equally to this work.

Notes

The authors declare no competing financial interest.

■ ACKNOWLEDGMENTS

■ REFERENCES

(1) Stranks, S. D.; Snaith, H. J. *Nat. Nanotechnol.* **2015**, *10*, 391−402.

(2) Srimath Kandada, A. R.; Petrozza, A. *Acc. Chem. Res.* **2016**, *49*, 536−544.

(3) D'Innocenzo, V.; Grancini, G.; Alcocer, M. J. P.; Kandada, A. R. S.; Stranks, S. D.; Lee, M. M.; Lanzani, G.; Snaith, H. J.; Petrozza, A. *Nat. Commun.* **2014**, *5*, 3486.

(4) Miyata, A.; Mitioglu, A.; Plochocka, P.; Portugall, O.; Wang, J. T.-W.; Stranks, S. D.; Snaith, H. J.; Nicholas, R. J. *Nat. Phys.* **2015**, *11*, 582−587.

(5) Saba, M.; Quochi, F.; Mura, A.; Bongiovanni, G. *Acc. Chem. Res.* **2016**, *49*, 166−173.

(6) Akkerman, Q. A.; D'Innocenzo, V.; Accornero, S.; Scarpellini, A.; Petrozza, A.; Prato, M.; Manna, L. *J. Am. Chem. Soc.* **2015**, *137*, 10276−10281.

(7) Yakunin, S.; Protesescu, L.; Krieg, F.; Bodnarchuk, M. I.; Nedelcu, G.; Humer, M.; De Luca, G.; Fiebig, M.; Heiss, W.; Kovalenko, M. V. *Nat. Commun.* **2015**, *6*, 8056.

(8) Deschler, F.; Price, M.; Pathak, S.; Klintberg, L. E.; Jaraush, D.-D.; Higler, R.; Huttner, S.; Leitjens, T.; Stranks, S. D.; Snaith, H. J.; Atature, M.; Phillips, R. T.; Friend, R. H. *J. Phys. Chem. Lett.* **2014**, *5*, 1421−1426.

(9) D'Innocenzo, V.; Srimath Kandada, A. R.; De Bastiani, M.; Gandini, M.; Petrozza, A. *J. Am. Chem. Soc.* **2014**, *136*, 17730−17733.

(10) Milot, R. L.; Eperon, G. E.; Snaith, H. J.; Johnston, M. B.; Herz, L. M. *Adv. Funct. Mater.* **2015**, *25*, 6218−6227.

(11) Yamada, Y.; Nakamura, T.; Endo, M.; Wakamiya, A.; Kanemitsu, Y. *J. Am. Chem. Soc.* **2014**, *136*, 11610−11613.

(12) Saba, M.; Cadelano, M.; Marongiu, D.; Chen, F.; Sarritzu, V.; Sestu, N.; Figus, C.; Aresti, M.; Piras, R.; Geddo Lehmann, A.; Cannas, C.; Musinu, A.; Quochi, F.; Mura, A.; Bongiovanni, G. *Nat. Commun.* **2014**, *5*, 5049.

(13) Stranks, S. D.; Burlakov, V. M.; Leijtens, T.; Ball, J. M.; Goriely, A.; Snaith, H. J. *Phys. Rev. Appl.* **2014**, *2*, 34007.

(14) Baumann, A.; Väth, S.; Rieder, P.; Heiber, M. C.; Tvingstedt, K.; Dyakonov, V. *J. Phys. Chem. Lett.* **2015**, *6* (12), 2350−2354.

(15) Buin, A.; Comin, R.; Xu, J.; Ip, A. H.; Sargent, E. H. *Chem. Mater.* **2015**, *27*, 4405−4412.

(16) Agiorgousis, M. L.; Sun, Y.; Zeng, H.; Zhang, S. *J. Am. Chem. Soc.* **2014**, *136*, 14570−14575.

(17) Duan, H.-S.; Zhou, H.; Chen, Q.; Sun, P.; Luo, S.; Song, T.-B.; Bob, B.; Yang, Y. *Phys. Chem. Chem. Phys.* **2015**, *17*, 112−116.

(18) Jung, M.-C.; Lee, Y. M.; Lee, H.-K.; Park, J.; Raga, S. R.; Ono, L. K.; Wang, S.; Leyden, M. R.; Yu, B. D.; Hong, S.; Qi, Y. *Appl. Phys. Lett.* **2016**, *108*, 073901.

(19) Kim, J.; Lee, S. H.; Lee, J. H.; Hong, K. H. *J. Phys. Chem. Lett.* **2014**, *5*, 1312−1317.

(20) Wetzelaer, G. J. A. H.; Scheepers, M.; Sempere, A. M.; Momblona, C.; Avila, J.; Bolink, H. J. *Adv. Mater.* **2015**, *27*, 1837−1841.

(21) Wen, X.; Feng, Y.; Huang, S.; Huang, F.; Cheng, Y.; Green, M.; Ho-baillie, A. *J. Mater. Chem. C* **2016**, *4*, 793−800.

(22) Fang, X.; Zhang, K.; Li, Y.; Yao, L.; Zhang, Y.; Wang, Y.; Zhai, W.; Tao, L.; Du, H.; Ran, G. *Appl. Phys. Lett.* **2016**, *108*, 071109.

(23) Leijtens, T.; Srimath Kandada, A. R.; Eperon, G.; Grancini, G.; D'Innocenzo, V.; Ball, J. M.; Stranks, S. D.; Snaith, H. J.; Petrozza, A. *J. Am. Chem. Soc.* **2015**, *137*, 15451−15459.

(24) Fang, H.-H.; Wang, F.; Adjokatse, S.; Zhao, N.; Loi, M. A. *Adv. Funct. Mater.* **2016**, *26*, 4653.

(25) Aristidou, N.; Sanchez-Molina, I.; Chotchuangchutchaval, T.; Brown, M.; Martinez, L.; Rath, T.; Haque, S. A. *Angew. Chem., Int. Ed.* **2015**, *54*, 8208−8212.

(26) von der Linde, D.; Kuhl, J.; Rosengart, E. *J. Lumin.* **1981**, *24/25*, 675−678.

(27) Borgwardt, M.; Sippel, P.; Eichberger, R.; Semtsiv, M. P.; Masselink, W. T.; Schwarzburg, K. *J. Appl. Phys.* **2015**, *117*, 215702.

(28) Rosen, D.; Doukas, A. G.; Budansky, Y.; Katz, A.; Alfano, R. R. *Appl. Phys. Lett.* **1981**, *39*, 935−937.

(29) Cho, H.; Jeong, S.-H.; Park, M.-H.; Kim, Y.-H.; Wolf, C.; Lee, C.-L.; Heo, J. H.; Sadhanala, A.; Myoung, N.; Yoo, S.; Im, S. H.; Friend, R. H.; Lee, T.-W. *Science* **2015**, *350* (6265), 1222−1225.

(30) Filippetti, A.; Delugas, P.; Mattoni, A. *J. Phys. Chem. C* **2014**, *118*, 24843−24853.

(31) Yin, W.-J.; Shi, T.; Yan, Y. *Appl. Phys. Lett.* **2014**, *104*, 063903.

(32) Du, M. H. *J. Mater. Chem. A* **2014**, *2*, 9091.

(33) Shi, H.; Du, M. H. *Phys. Rev. B: Condens. Matter Mater. Phys.* **2014**, *90*, 174103.

(34) Du, M.-H. *J. Phys. Chem. Lett.* **2015**, *6*, 1461−1466.

(35) Trankle, G.; Leier, H.; Forchel, A.; Haug, H.; Ell, C.; Weimann, G. *Phys. Rev. Lett.* **1987**, *58*, 419−422.

(36) Akkerman, Q. A.; Motti, S. G.; Srimath Kandada, A. R.; Mosconi, E.; D'Innocenzo, V.; Bertoni, G.; Marras, S.; Kamino, B. A.; Miranda, L.; De Angelis, F.; Petrozza, A.; Prato, M.; Manna, L. *J. Am. Chem. Soc.* **2016**, *138*, 1010−1016.

(37) Makarov, N. S.; Guo, S.; Isaienko, O.; Liu, W.; Robel, I.; Klimov, V. I. *Nano Lett.* **2016**, *16*, 2349−2362.

(38) Klimov, V. *J. Phys. Chem. B* **2000**, *104*, 6112−6123.

(39) Because the PLQY is about 75% even at low excitation, due to other nonradiative recombination processes, we rescaled $\langle N \rangle$ accordingly to account for this loss channel.